BEST PAPER AWARD in Industrial and Congeneration

Proceedings of GT2010
ASME Turbo Expo 2010: Power for Land, Sea and Air
June 14-18, Glasgow, UK

GT2010-23722

3D Modeling for Wet-compression in a Single Stage Compressor Including Liquid Particle Erosion Analysis

Jobaidur R. Khan and Ting Wang
Energy Conversion & Conservation Center
University of New Orleans
New Orleans, LA 70148-2220

ABSTRACT

Gas turbine inlet fog / overspray cooling is considered as a simple and effective method to increase power output. To help understand the water mist transport in the compressor flow passage, this study conducts a 3-D computational simulation of wet compression in a single rotor-stator compressor stage using the commercial code, Fluent. A sliding mesh scheme is used to simulate the stator-rotor interaction in a rotating frame. Eulerian-Lagrangian method is used to calculate the continuous phase and track the discrete (droplet) phase respectively. Models to simulate droplet breakup and coalescence are incorporated to take into consideration the effect of local acceleration and deceleration on water droplet dynamics. Analysis on droplet history (trajectory and size) with stochastic tracking is employed to interpret the mechanism of droplet dynamics under the influence of local turbulence, acceleration, diffusion, and body forces. An liquid-droplet erosion model is included. The sensitivity of turbulence models on the results is conducted by employing 6 different turbulence models and 4 different time constants.

The result shows that the local thermal equilibrium is not always achieved due to short residence time and high value of latent heat of water. Local pressure gradients in both the rotor and stator flow passages drive up the droplet slip velocity during compression. The erosion model predicts that the most eroded area occurs in leading edge and one spot of trailing edge of the rotor suction side.

NOMENCLATURE

C	Concentration (kg/m^3)
C_t	Particle stochastic tracking time constant
c_p	Specific heat (J/kg-K)
D	Mass diffusion coefficient (m^2/s)
d	Droplet diameter (m)
d_{sp}	Spring Damping Coefficient (N-s/m)
F	Force (N)
F_{sp}	Spring force (N)
k	Turbulence kinetic energy (m^2/s^2)
k_c	Mass transfer coefficient (m/s)
k_{sp}	Spring Constant (N/m)
h	Convective heat transfer coefficient (W/m^2-K)
h_{fg}	Latent heat (J/kg)
m	Mass (kg)
Nu	Nusselt number, hd/λ
P	Static pressure (N/m^2)
P_o	Total pressure (N/m^2)
Pr	Prandtl number, ν/α
RH	Relative humidity (%)
Re	Reynolds number, ud/ν
Sc	Schmidt number (ν/D)
Sh	Sherwood number (k_cd/D)
T	Temperature (K, ^{o}F)
t	Time (s)
u	Streamwise velocity component (m/s)
u', T', C'	Turbulence fluctuation terms
v	Spanwise velocity component (m/s)
x, y, z	Coordinates (m)

Greek

α	Thermal diffusivity (m^2/s)
ω	Specific dissipation rate (1/s)
ε	Turbulence dissipation rate (m^2/s^3)
λ	Heat conductivity (W/m-K)
μ	Dynamic viscosity (kg/m-s)
ν	Kinematic viscosity (m^2/s)
ρ	Density (kg/m^3)
τ	Stress tensor (kg/m-s^2)
σ	Surface Tension (N/m)

Subscript

a	Air
aw	Adiabatic wall
c	Coolant
g	Hot gas/air

i,j,k	Indices of direction
in	Inlet
p	Particle or droplet
t	Turbulent
w	Water phase
x	x-direction (axial)
o	Cooling without mist
∞	Far away from droplets

INTRODUCTION

It is always extremely important and required by law for a utility company to meet the peak-load demand during hot weather conditions. Land based gas turbines (GT) are often used to meet these demands. However, power output and efficiency of gas turbines are reduced significantly during the summer because the air becomes lighter (which results in less mass flow rate), and the compressor's power consumption increases with increased ambient temperature.

It has been estimated that every 1°F rise of ambient air temperature reduces the gas turbine output by approximately 0.3 to 0.5% [1]. To increase the power output as well as thermal efficiency, gas turbine inlet air-cooling is considered as the most convenient and cost-effective method. Among various cooling schemes, fog cooling (a direct evaporative cooling) has gained increasing popularity due to its simplicity and low installation cost at approximately $40-60/kW. During fog cooling, demineralized water is atomized to micro-scaled droplets (or mist in the size of 10-20 μm diameter) and introduced to the inlet airflow. The following is a brief summary of related studies.

Bhargava and Meher-Homji [2] presented the results of a comprehensive parametric analysis on the effect of inlet fogging on a wide range of existing gas turbines. They analyzed both evaporative and overspray fogging conditions. They showed that the performance parameters indicative of inlet fogging effects have a definitive correlation with key gas turbine design parameters. In addition, they indicated that aero-derivative gas turbines, in comparison to the industrial machines, have a higher performance improvement due to the inlet fogging effects.

Chaker et. al. [3-5] presented the results of extensive experimental and theoretical studies conducted over several years and coupled with practical aspects learned in the implementation of nearly 500 inlet fogging systems on gas turbines ranging from 5 to 250 MW. They studied the underlying theory of droplet thermodynamics and heat transfer and provided practical points relating to the implementation and application of inlet fogging to gas turbine engines. They also described the different measurement techniques (for droplets) available to design nozzles and provided experimental data on different nozzles. They strongly recommended that a standardized nozzle testing method for gas turbines be established by the industry.

To improve understanding of the fundamental physics of gas turbine inlet fogging, several studies have been conducted via two-phase flow simulation. Payne and White [6] developed a computational method to solve two-phase (air-water mixture) flow, including the evaporative cooling. Their results show that the axial velocity in the compressor is reduced due to the progressive droplet evaporation, which affects the flow incidence onto successive blade rows, and as a result, the blade pressure distributions are changed. From the global point of view, stage pressure increases under wet compression.

Bianchi et. al. [7] showed the influence of water droplet diameter and surface temperature effect on gas turbine performance. They redrew the performance maps for axial compressor under the influence of water injection. They have shown that the GT power output increases as the diameter of droplets decreases and water temperature increases.

As the interest in burning alternative clean fuels increases, Khan and Wang [8] specifically investigated the inlet fogging on the gas turbine system performance by using low calorific value (LCV) synthetic fuels derived from biomass and coal gasification.

Khan and Wang [9, 10] further extended the program to develop stage-by-stage wet-compression theory for overspray and interstage fogging that includes the analysis and effect of pre-heating and pre-cooling at each small stage inside the compressor. An algorithm has been developed using the thermal equilibrium method to calculate local velocity diagram and perform one-dimensional stage-by-stage analysis of the inlet and interstage fogging effect on airfoil aerodynamics and loading. Khan and Wang [11] extended the equilibrium model to the non-equilibrium model in which the water droplets evaporation depends on the hydrodynamic and thermal residence times and may not reach saturation at the end of stage.

Considering the large variation of the CFD results due to various two-phase and turbulence models incorporated in a typical computational code. Li and Wang [12] conducted a study focusing on examining the effects of these models on mist/air film cooling effectiveness on the turbine blade. They have tested the cooling by changing turbulence models, turbulence intensity, different forces acting upon the droplets, droplet sizes, particle tracking numbers, etc. They found the RSM (Reynolds Stress Model) and standard k-ε turbulence models produced consistent results. Stochastic tracking of droplets provided significant change of the heat transfer and cooling effectiveness.

Wang and Dhanasekaran [13] calibrated a CFD model for mist/steam impinging jet to the cool turbine blade, by employing different turbulence models, computational cells, wall y^+ values, and selection of near-wall functions using the laboratory results. They also studied the effect of different forces (e.g. drag, thermophoretic, Brownian, and Saffman's lift force). They found that the standard k-ε and RSM turbulence models had produced the closest results to the experimental data.

Zheng et. al. [14] conducted a wet compression simulation over one stage of a compressor using the CFD software FLUENT with different amounts of water injection and different water droplet diameters. Their result showed that under fogging, the pressure ratio increased a little (1.0273 vs. 1.0269), and the compressor exit temperature decreased. They showed that the cooling effect was better for smaller droplets. They did not consider droplet breakup, coalescence and droplet erosion. The spray points were not documented.

Khan and Wang [15] investigated 2-D study of wet compression using the blade geometry of Hsu and Wo [16].

They incorporated droplet break-up and coalescence models and also propose a liquid particle erosion model. Although the 2-D CFD analysis is very informative, a 3-D analysis can provide more insight into droplet dynamics inside a rotating compressor stages. To this end, the objective of this paper is to use 3-D CFD simulation to investigate (a) the mechanism of droplet dynamics and air-droplet interactions in the compressor flow passage including droplet breakup and coalescence, (b) the effect of wet compression on local flow and thermal properties over the compressor blade, (c) sensitivity of using different turbulence models and different time constant for stochastic particle tracking, and (d) the potential erosion on blades.

NUMERICAL MODEL

Geometrical Configuration

Figure 1 shows the meshes of inlet, rotor and stator of the 3D computational domain. The mesh number is reduced for visual clarity in this figure. The 2-D geometries of rotor and stator are adopted from Hsu and Wo [16] and then extruded from the base up to the blade height. A 2% of the tip clearance for rotor is imposed here according to Chima [17] and Gerolymos and Vallet [18]. Figure 2(a) shows the periodic meshes of inlet, rotor and stator, and Fig. 2(b) shows the close-up view of one pitch (i.e. one periodic computational domain) of inlet, rotor and stator. Structured mesh is used in the inlet sub-domain and on the blade surfaces; tetrahedral meshes are used in rotor and stator sub-domains. To investigate grid sensitivity on the results, four different sizes of meshes are used for the baseline case (no fogging) and only one size of mesh is used for the fogging case due to limitation of existing computational capacity to track all the droplets. 0.225 million elements are used for both cases and 0.45, 0.9 and 1.7 million meshes are used for baseline case with no fogging.

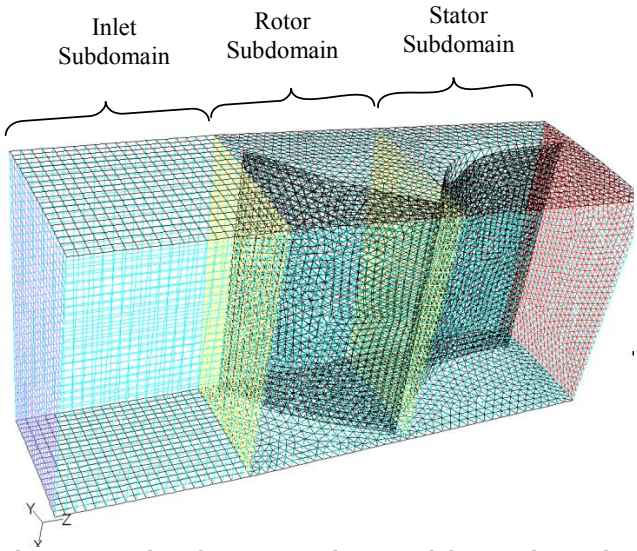

Figure 1 Meshes for rotor and stator. (The mesh number is reduced for visual clarity.)

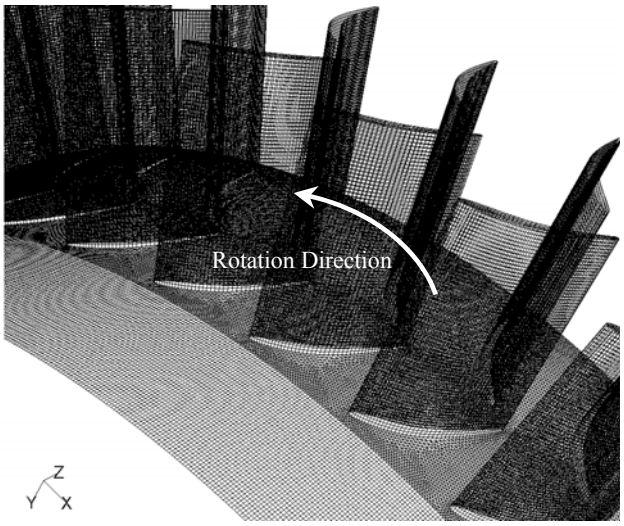

Figure 2(a) Periodic Meshes

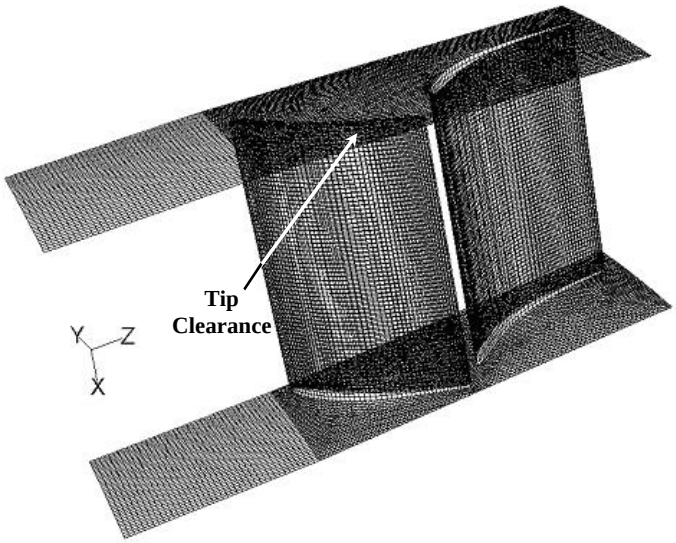

Figure 2(b) Close-up view of one pitch of inlet, rotor and stator

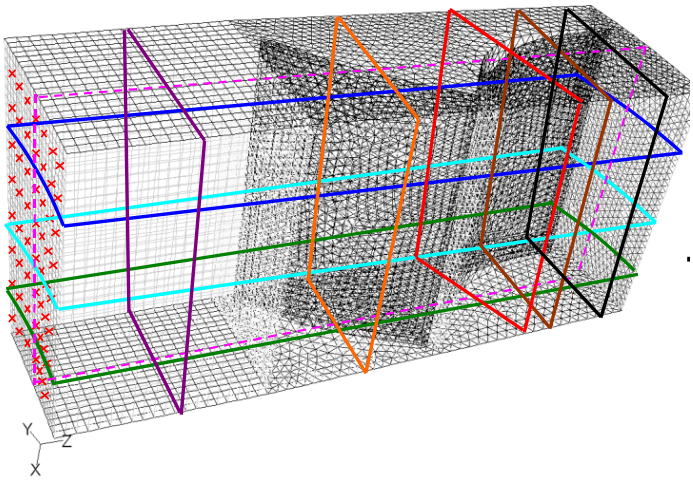

Figure 3 Selected surfaces for analysis (3 radial, 3 axial and one circumferential plane). The cross marks show the water injection locations

Figure 3 shows how the computational domain has been divided into three sub-domains: inlet sub-domain, rotor sub-domain and stator sub-domain. This figure also shows the selected surfaces for analysis and discussion including three radial surfaces (y-z planes at 25%, 50% and 75% of blade height respectively), three axial surfaces (x-y planes in the middle of each sub-domains) and one vertical circumferential surface (x-z plane) slicing through the middle of the pitch. The radial surfaces are named as radial-25, radial-50 and radial-75; axial surfaces are named as the developing-plane, rotor-plane and stator-plane; and the x-z vertical slicer is named as the pitch-plane. Fifty-six cross marks at the inlet of the domain show the locations of water injections. The domain extends axially from z = 0 to z = 0.18m (3 times the chord length), radially from x = –0.45m to x = –0.36m (1½ times the chord length) and circumferentially from –3.6° to +3.6° (or an angular span of 7.2°) for one pitch. A total of 50 pairs of rotors and stators is modeled by applying the periodic boundary on one pitch.

Water is sprayed at 56 points (8 radial × 7 circumferential), which are equally distant in radial and longitudinal directions at the inlet as shown in Fig. 3. The planes for three axial surfaces (maroon, orange and brown) are at z = 0.03m, z = 0.09m, and z = 0.15m respectively. These axial surfaces are axisymmetric to y = 0 plane and shown in Fig. 3. Two more planes are adopted for the analysis of secondary flow, which are colored as red and black in Fig. 3. Red plane is perpendicular to the stator at 20% of its chord length from the leading edge. The black plane is an axial plane (z = 0.165), which lies very close to the exit.

Figure 4 shows the velocity diagram of the blades used in this study according to one-dimensional mean line calculations. The rotor turning angle is 34.6° and stator turning angle is 49°.

Governing Equations

The 3-D, time-averaged, periodically steady-state Navier-Stokes equations as well as equations for mass, energy and species transport are solved. The transient governing equations for conservation of mass, momentum, and energy are given as:

$$\frac{\partial \rho}{\partial t} + \frac{\partial}{\partial x_i}\left(\rho u_i\right) = S_m \tag{1}$$

$$\frac{\partial}{\partial t}\left(\rho u_j\right) + \frac{\partial}{\partial x_i}\left(\rho u_i u_j\right) = \rho \vec{g}_j - \frac{\partial P}{\partial x_j} + \frac{\partial}{\partial x_i}\left(\tau_{ij} - \rho\overline{u'_i\, u'_j}\right) + F_j \tag{2}$$

$$\frac{\partial}{\partial t}\left(\rho c_p T\right) + \frac{\partial}{\partial x_i}\left(\rho c_p u_i T\right) = \frac{\partial}{\partial x_i}\left(\lambda \frac{\partial T}{\partial x_i} - \rho c_p \overline{u'_i\, T'}\right) + \mu\Phi + S_h \tag{3}$$

where τ_{ij} is the symmetric stress tensor defined as

$$\tau_{ij} = \mu\left(\frac{\partial u_j}{\partial x_i} + \frac{\partial u_i}{\partial x_j} - \frac{2}{3}\delta_{ij}\frac{\partial u_k}{\partial x_k}\right) \tag{4}$$

The source terms (S_m, F_j and S_h) are used to include the contributions of water vapor mass, droplet forces, and evaporation energy from the dispersed phase (water droplets). $\mu\Phi$ is the viscous dissipation, and λ is the heat conductivity. The specific heat (c_p) in the eq. (3) is calculated from the mass-weighted value of specific heat of the gas and liquid components present in the domain. The effect of temperature on c_p values is negligible within the studied range between 288 and 321°C.

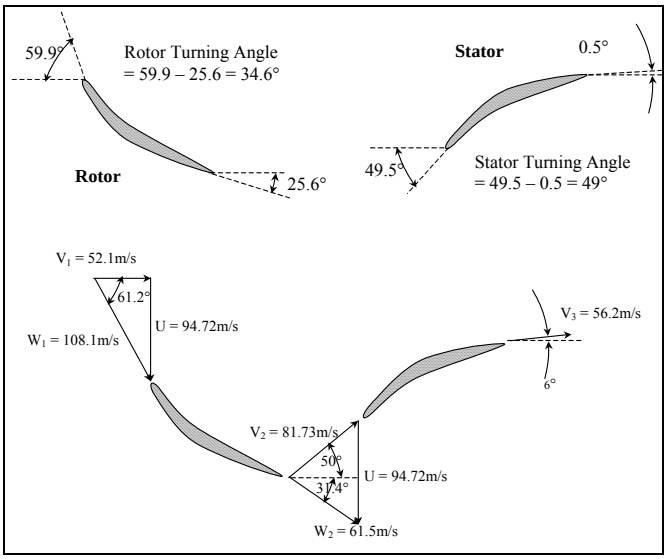

Figure 4 Flow and blade angles and the velocity diagrams at the mean diameter

During fog cooling, water droplets evaporate into vapor and the water vapor diffuses and transported into its surrounding flow. The flow mixture consists of three main species: water vapor (H_2O), oxygen (O_2) and nitrogen (N_2). The equation for species transport is

$$\frac{\partial}{\partial x_i}\left(\rho u_i C_j\right) = \frac{\partial}{\partial x_i}\left(\rho D_j \frac{\partial C_j}{\partial x_i} - \rho\overline{u'_i\, C'_j}\right) + S_j, \tag{5}$$

where C_j is the mass fraction of the species (j) in the mixture, and S_j is the source term for this species. D_j is the diffusion coefficient.

Note that the terms of $\rho\,\overline{u'_i u'_j}$, $\rho c_p\,\overline{u'_i\, T'}$, and $\rho\,\overline{u'_i\, C'_j}$ represent the Reynolds stresses, turbulent heat fluxes and turbulent concentration (or mass) fluxes, which should be modeled properly for a turbulent flow.

Turbulence Models

Wang and Dhanasekaran [13] investigated the effect of different turbulence models on the two-phase mist transports in the slot impinging jet on a flat surface. They reported that the RSM turbulence model provided the results most consistent with the experimental data and the standard k-ε turbulence model was proven robust with good results only next to the RSM model. In this paper, a sensitivity study of using six different turbulence models is conducted and results are consistent with Dhanasekaran and Wang's finding. Since the RSM model requires an order of magnitude of computational time over the k-ε model, the standard k-ε model is therefore used with the enhanced near-wall treatment to significantly reduce the computational time but maintain the uncertainty within acceptable range of ±10 ~15 %.

Standard k-ε Model – The standard k-ε model, based on the Boussinesq hypothesis, relates the Reynolds stresses to the mean velocity as

$$-\rho\overline{u'_i u'_j} = \mu_t\left(\frac{\partial u_i}{\partial x_j}+\frac{\partial u_j}{\partial x_i}\right)-\frac{2}{3}\rho k\delta_{ij} \quad (6)$$

where k is the turbulent kinetic energy, and μ_t is the turbulent viscosity given by

$$\mu_t = \rho C_\mu k^2/\varepsilon \quad (7)$$

where C_μ is a constant, and ε is the dissipation rate. The equations for the turbulent kinetic energy (k) and the dissipation rate (ε) are:

$$\frac{\partial}{\partial t}(\rho k)+\frac{\partial}{\partial x_i}(\rho u_i k)=\frac{\partial}{\partial x_i}\left[\left(\mu+\frac{\mu_t}{\sigma_k}\right)\frac{\partial k}{\partial x_i}\right]+G_k-\rho\varepsilon \quad (8)$$

$$\frac{\partial}{\partial t}(\rho\varepsilon)+\frac{\partial}{\partial x_i}(\rho u_i\varepsilon)=\frac{\partial}{\partial x_i}\left[\left(\mu+\frac{\mu_t}{\sigma_\varepsilon}\right)\frac{\partial\varepsilon}{\partial x_i}\right]+C_{1\varepsilon}G_k\frac{\varepsilon}{k}-C_{2\varepsilon}\rho\frac{\varepsilon^2}{k} \quad (9)$$

The term G_k is the generation of turbulence kinetic energy due to the mean velocity gradients.

The turbulent heat flux and mass flux can be modeled with the turbulent heat conductivity (λ_t) and the turbulent diffusion coefficient (D_t), respectively.

$$\rho c_p\overline{u'_i T'} = -\lambda_t\frac{\partial T}{\partial x_i} = -c_p\frac{\mu_t}{Pr_t}\frac{\partial T}{\partial x_i} \quad (10)$$

$$\rho\overline{u'_i C'} = -\rho D_t\frac{\partial C}{\partial x_i} = -\frac{\mu_t}{Sc_t}\frac{\partial C}{\partial x_i} \quad (11)$$

The constants $C_{1\varepsilon}$, $C_{2\varepsilon}$, C_μ, σ_k, and σ_ε used are: $C_{1\varepsilon} = 1.44$, $C_{2\varepsilon} = 1.92$, $C_\mu = 0.09$, $\sigma_k = 1.0$, $\sigma_\varepsilon = 1.3$ [19]. The turbulence Prandtl number, Pr_t, is set to 0.85, and the turbulence Schmidt number, Sc_t, is set to 0.7.

Enhanced Wall Function – The above k-ε model is mainly valid for high Reynolds number fully-turbulent flow. Special treatment is needed in the region close to the wall. The enhanced wall function is one of several methods that model the near-wall flow. In the enhanced wall treatment, the two-layer model is combined with the wall functions. The whole domain is separated into a viscosity-affected region and a fully turbulent region by defining a turbulent Reynolds number, Re_y,

$$Re_y = y k^{1/2}/\nu \quad (12)$$

where k is the turbulence kinetic energy and y is the distance from the wall. The standard k-ε model is used in the fully turbulent region where $Re_y > 200$, and the one-equation model of Wolfstein [20] is used in the viscosity-affected region with $Re_y < 200$. The turbulent viscosities calculated from these two regions are blended with a blending function (θ) to smoothen the transition.

$$\mu_{t,enhanced} = \theta\mu_t + (1-\theta)\mu_{t,l} \quad (13)$$

where μ_t is the viscosity from the k-ε model of high Reynolds number, and $\mu_{t,l}$ is the viscosity from the near-wall one-equation model. The blending function is defined; so it is equal to 0 at the wall and 1 in the fully turbulent region. The linear (laminar) and logarithmic (turbulent) laws of the wall are also blended to make the wall functions applicable throughout the entire near-wall region.

Dispersed-Phase Model (Water Droplets)

Droplet Flow and Heat Transfer – Based on the Newton's 2nd Law, droplets motion in the airflow can be formulated by

$$\dot{m}_p d\mathbf{v_p}/dt = \sum\mathbf{F} = F_D + F_g + F_P + F_s \quad (14)$$

where m_p is the droplet mass, and v_p is the droplet velocity (vector). The right-hand side is the combined force acted on the droplets, which are F_D (drag force), F_g (gravity and buoyancy force), F_P (pressure force), F_S (Saffman lift force) etc. The following are the parameters for magnitude order of various forces for the present study. The density ρ_p and size d_p of particle are 998.2 kg/m^3 and 10μm, respectively. The air density ρ_a is 1.23 kg/m^3, and its dynamic viscosity coefficient μ are 1.85×10^{-5} kg/(m·s). The average value of pressure gradient $\partial p/\partial x$ is about 2.4×10^4 Pa/m. The maximum value of (u_a-u_p) is near 50 m/s, where u_p and u_a the velocity of particle and air, respectively; the average value $d(u_a-u_p)/dt$ is about 50,000 m/s². $f(Re_p) \sim 4.76$. Taking the above conditions into account, the magnitude order of various forces can be acquired following Wang et. al.'s [21] study.

$$F_D = -3\pi d_p\mu(u_p-u_a)\, f(Re_p) \sim 4.6\times10^{-7} \quad (15.1)$$

$$F_g = \frac{1}{6}\pi d_p^3(\rho_p-\rho_a)g \sim 5\times10^{-12} \quad (15.2)$$

$$F_P = -\frac{1}{6}\pi d_p^3\frac{\partial P}{\partial x} \sim 2.6\times10^{-11} \quad (15.3)$$

$$F_s = 1.61(\mu\rho_a)^{\frac{1}{2}}d_p^2(u_a-u_p)\left|\frac{\partial u_a}{\partial y}\right|^{\frac{1}{2}} \sim 1.9\times10^{-8} \quad (15.4)$$

where, g is the gravitational acceleration, Re_p is the droplet Reynolds number and $f(Re_p)$ is the correction factor for Stokes-drag force, which are expressed as,

$$Re_p = \frac{\rho_a|u_a-u_p|d_p}{\mu} \quad (16)$$

and

$$f(Re_p) = C_D\,Re_p/24 \quad (17)$$

According to the Stokes law for $Re_p < 1$, $C_D\,Re_p/24 = 1$. There are many models to formulate the term $C_D\,Re_p/24$ for higher particle Reynolds number. Schiller and Naumann [22] correlated the expression up to Re = 800 as,

$$\frac{C_D\,Re_P}{24} = 1+0.15Re_p^{0.687} \quad (18)$$

Without considering the radiation heat transfer, droplet's heat transfer depends on convection, and evaporation is given as

$$m_p c_p\frac{dT}{dt} = \pi d^2 h(T_\infty - T)+\frac{dm_p}{dt}h_{fg} \quad (19)$$

where h_{fg} is the latent heat. The convective heat transfer coefficient (h) can be obtained with an empirical correlation [23-24]:

$$Nu_d = \frac{hd}{\lambda} = 2.0+0.6\,Re_p^{0.5}\,Pr^{0.33} \quad (20)$$

where Nu is the Nusselt number, and Pr is the Prandtl number.

The mass change rate or vaporization rate in Eq. (19) is governed by concentration difference between droplet surface and the air stream,

$$-\frac{dm_p}{dt} = \pi d^2 k_c(C_s - C_\infty) \quad (21)$$

where k_c is the mass transfer coefficient, and C_s is the vapor concentration at the droplet surface, which is evaluated by assuming the flow over the surface is saturated. C_∞ is the vapor concentration of the bulk flow, and is obtained by solving the species transport equations. The values of k_c can be given from a correlation similar to Eq. (21) by [23-24].

$$Sh_p = \frac{k_c d}{D} = 2.0 + 0.6 Re_p^{0.5} Sc^{0.33} \quad (22)$$

where Sh is the Sherwood number, Sc is the Schmidt number (defined as ν/D), and D is the diffusion coefficient of vapor in the bulk flow.

When the droplet temperature reaches the boiling point, the following equation can be used to evaluate its evaporation rate [25]:

$$-\frac{dm_p}{dt} = \pi d^2 \left(\frac{\lambda}{d}\right)(2.0 + 0.46 Re_p^{0.5}) \ln\left(1 + c_p (T_\infty - T)/h_{fg}\right)/c_p \quad (23)$$

where λ is the gas/air heat conductivity, and c_p is the specific heat of the bulk flow.

Theoretically, evaporation can occur at two stages: (a) when the temperature is higher than the saturation temperature (based on local water vapor concentration), water evaporates, and the evaporation is controlled by the water vapor partial pressure until 100% relative humidity is achieved; (b) when the boiling temperature (determined by the air-water mixture pressure) is reached, water continues to evaporate. After the droplet evaporates due to either high temperature or low moisture partial pressure, the water vapor is transported away due to convection and diffusion as described in the water vapor species transport equation (5).

Stochastic Particle Tracking - The turbulence effect on droplets dispersion is considered by using stochastic tracking. Basically, the droplet trajectories are calculated by using the instantaneous flow velocity ($\bar{u} + u'$) rather than the average velocity ($\bar{u}$). The velocity fluctuations are then given as:

$$u' = \varsigma\left(\overline{u'^2}\right)^{0.5} = \varsigma(2k/3)^{0.5} \quad (24)$$

where ζ is a normally distributed random number [25]. This velocity will apply during the characteristic lifetime of the eddy ($t_e = C_t(k/\varepsilon)$), where C_t is a time constant to be specified according to the turbulent flow structure and the behavior of droplet dynamics. After this time period, the instantaneous velocity will be updated with a new ζ value until a full trajectory is obtained.

Droplet Dynamics – Khan and Wang [15] made a 2-D CFD simulation for wet compression. They incorporated models to simulate droplet breakup and coalescence to take into consideration the effect of local acceleration and deceleration on water droplet dynamics. Taylor Analogy Breakup (TAB) model [26] was employed in that study and is adopted in the present study as well. The TAB model is a classic method for calculating droplet breakup, which is applicable to many engineering sprays. This method is based upon Taylor's analogy [26] between an oscillating and distorting droplet and a spring mass system, where the surface tension forces, droplet drag force and droplet viscosity forces are analogized with restoring, external, and damping forces.

Khan and Wang [15] used the O'Rourke coalescence model [27] in their study, which is also adopted in this study. O'Rourke considered coalescence as an outcome of collision. O'Rourke's algorithm assumes that two droplets may collide only if they are in the same continuous-phase cell. This assumption can prevent droplets that are quite close to each other, but not in the same cell, from colliding, although the effect of this error is lessened by allowing some droplets that are farther apart to collide. The overall accuracy of the scheme is second-order in space. Once it is determined that two parcels collide, the outcome of the collision is "coalescence" if the droplets collide head on, and "bouncing" if the collision is more oblique. Droplet coalescence model improves discrete phase calculation when strong local acceleration or deceleration presents in the flow field such as over the airfoil surface.

Erosion Model

When the droplet flows in the air stream and hits the compressor blades (stator and rotor), the blades may encounter erosion or accretion. Studying potential water droplet induced erosion can borrow the experience encountered in the steam turbine. Water droplet erosion poses a serious potential threat to the critical path of maintenance outages in steam turbine. Lam et. al. [28] estimated erosion rate in steam turbines from empirical formula. They presented two applications for the demonstration of erosion rates. Their results showed that the large droplets impact on the leading edge suction side due to insufficient axial clearance for the droplets to break up. Their other case handled with extremely wet steam, which was developed by a film of water accumulated on the stationary blades. Although the film got enough space for breaking up, higher liquid droplet density had caused the premature erosion nonetheless.

Erosion is significantly dependent on the attack angle. Haugen et. al. [29] tested a total of 28 materials at impact angles of 22.5° and 90°, and some at 7.5°, with test air velocities at 22, 55 and 320 m/s. Carbon Steel was selected as a reference material and was, as such, subject to more extensive examination than the other materials. Additional tests were also performed at impact angles of 15°, 30° and 45°. The maximum erosions were found at impact angles 22.5° and 90° for ductile and brittle materials, respectively. The basic premise was that the cutting action of the particles is more important for ductile materials and deformation (or displacement) is more significant for brittle materials. Of the 28 materials, the most erosion resistant were found to be the three solid tungsten carbide materials and two of the ceramics, Si_3N and B_4C. Only one coating, a Degun tungsten carbide layer, was found to give significantly improved erosion characteristics as compared with the reference material, Carbon Steel.

Nokleberg et. al. [30] studied the erosion of the choke valve used in oil and gas industry. They used a Lagrangian trajectory calculation with stochastic tracking to account for the effect of local turbulence quantities predicted in the continuous phase (k-ε model) for their erosion model. The forces on the particles included drag force, gravity and pressure. Three different choke openings were simulated with flow, particle tracking and erosion: 10%, 12.5% and 25% open. In addition the flow field was simulated for 50% choke opening. A velocity restitution factor after wall impact (normal velocity ratio) of 90% was used. The erosion tests in both the modified Needle & Seat choke and the External Sleeve choke gave peak erosion rates only 2-3 times larger than calculated. This was near the uncertainty of the erosion model alone. Other uncertainties were particle sharpness and reflection velocities after several impacts in the chokes. The predicted behavior was thus satisfactory for such complex

flow geometries, especially since there was such a large difference in the maximum erosion rate for the two types of chokes for the same test condition.

Considering all the above mentioned effects, the rate of erosion (kg/m^{2}s) is formulated as,

$$R = \frac{\dot{m}_p K f(\alpha) V^n}{A_{face}} \quad (25)$$

Where, K is a Material constant, α is the impact angle of the particle path with the wall face, $f(\alpha)$ is a function of impact angle, V is the relative particle velocity, n is a constant, and A_{face} is the area of the cell face at the wall. Nokleberg and Sontvedt [30] used this model and found the erosion tests gave peak erosion rates 2-3 times larger than calculated as mentioned earlier. They reasoned that this large difference was contributed by the variations of surface geometry, particle sharpness and reflection velocities after several impacts in the chokes. They suggested the value of $f(\alpha)$ in a piecewise linear manner between three data points for ductile materials as: $f(0°) = 0$, $f(20°) = 1.0$, and $f(90°) = 0.3$ and two points linear relationship for brittle materials between $f(0°) = 0$ and $f(90°) = 1.0$.

Most of the published data have been for solid-particle erosion. The data related to erosion caused by liquid-droplet impact is scarce. Bowden and Field [31] showed that the stress pulse produced by high-speed liquid impact is intense and of a duration of only 1 or 2μs. On the other hand, a solid-to-solid impact has, by comparison, a much longer impact time by hundreds of microseconds. Based on this discovery, it is assumed in the present study that the K value for the liquid droplets is about two orders of magnitude less than solid's K value. Therefore, K is selected as 2×10^{-11}, which is $1/100^{th}$ of the steel's K value. n is selected as 2.6 and $f(\alpha)$ is modeled by the piecewise linear approach between three data points: $f(0°) = 0$, $f(20°) = 1.0$, and $f(90°) = 0.3$ as stated earlier.

Keating and Nesic [32] explained that the normal velocity is responsible for liquid particle erosion. They also introduced a critical threshold velocity for which erosion initiates, below which no erosion takes place. Based on their study, the present model further incorporates the normal component of velocity ($V\sin\alpha$) and the critical threshold velocity (V_{cr}) into Eq (25) as.

$$R = \begin{cases} \dfrac{\dot{m}_p K f(\alpha)(V\sin\alpha - V_{cr})^n}{A_{face}} & (V\sin\alpha \geq V_{cr}) \\ 0 & (V\sin\alpha < V_{cr}) \end{cases} \quad (26)$$

V_{cr} is the critical velocity below which erosion does not take place. The critical velocities for erosion initiation for different materials were reported by Bitter [33, 34] and the critical velocity for steel was 0.668m/s. Erosion model built in the FLUENT is a solid particle erosion model, so an user defined function (UDF) is written to incorporate Eq. 26 into our model.

Boundary Conditions

Continuous Phase – The stagnation condition of the inlet main flow is assigned as 1 atm air at 304.2K (to maintain a static temperature of 300K), and 60% RH (or with the absolute humidity at 0.01369 kg/kg dry air) moving at a uniform velocity of 92 m/s. The inlet condition is assigned by fixing the total pressure as 101.325 kPa and total temperature at 304.2 K, and the exit condition is assigned by fixing the static pressure at a value that will give the inlet velocity of 92 m/s. Since the exit static pressure is not known, iteration will take place to try different exit pressures until the inlet velocity reaches an average value of 92 m/s. Under these assigned conditions, the inlet static pressure, static temperature, and velocity will be calculated cell by cell and will not be uniform, but the stagnation pressure is always uniformly maintained at the initialized value of 101.325 kPa. There was an attempt to assign a uniform velocity at the inlet. However, if a uniform velocity was assigned as the inlet condition, the total pressure would be calculated cell-by-cell and would not be uniform, which is not consistent with reality.

The chilled water at 288K (58^{o}F) is atomized and injected at a velocity of 25 m/s. The calculated mass flow rate is 0.472 kg/s per pitch, which is used to determine the amount of water, 0.00472 kg/s, needed for achieving 1% overspray fogging case.

The static pressure at the inlet is calculated mesh by mesh, so it is nonuniformly distributed, with an average value of 96.4 kPa to have the desired inlet velocity (92m/s) with a flow coefficient of 0.6. Since there are 50 rows of blades, the rotational periodic (or cyclic) boundary condition is set to simulate 50 rows of rotors and stators. The total mass flow rate for the entire compressor inlet is $(0.472 \times 50) = 23.6$ kg/s for fogging.

The backflow (reverse flow) temperature (if any) is set to 310 K. All the walls (rotor and stator) in the computational domain are assigned as adiabatic with the non-slip velocity boundary condition, i.e zero velocity at all walls. As the compressor has 50 rows of blades, the included angle between two consecutive blade rows is 7.2°. Again, all the parameters are set with rotational periodic boundary conditions, which carry the information from the downward edge to the forward edge along the rotating direction.

Dispersed Phase -- The droplet size is uniformly given as 10μm. Although in the real overspray applications, the water droplet sizes posses a nonuniform distribution, for the purpose of a easy tracking of droplet size variations during the course of evaporation, using uniform droplet size provides a convenient controlling tool.

The boundary condition for droplets at the walls can be assigned as either reflected, trapped, or maintaining as a liquid film. Usually, when the wall temperature is 28°C (=50°F) above the water saturation temperature (i.e. at 28^{o}C superheat), the water droplets do not stick to the wall surface; it reflects from the surface. This situation occurs in the later stages of the compressor, but not in the first stage as simulated in the present study. However, since the blade surfaces move very fast, the impact force induced when the droplets collide with the surface may bounce off the droplets. In the meantime, the water droplets could also stick to the surface and form a liquid film [35]. Since all three conditions could occur in the real application but Fluent code only allows one condition to be assigned at a time, this study employs both reflected and filmed boundary conditions at separated cases and the results are compared. The results of the trapped condition should be between the results of

reflected and filmed conditions because it allows water droplets to evaporate when they hit the surfaces. At the outlet, the droplets just simply flee/escape from the computational domain.

Numerical Method

The commercial software package FLUENT (version 6.2.16) from Ansys, Inc. is adopted for this study. The simulation uses the segregated solver, which employs an implicit pressure-correction scheme and decouple the momentum and energy equations according to the FLUENT manual [36]. The SIMPLE algorithm is used to couple the pressure and velocity. Second order upwind scheme is selected for spatial discretization of the convective terms and species. Langrangian trajectory calculations are employed to model the dispersed phase of droplets. The impact of droplets on the continuous phase is considered as source terms to the governing equations. After obtaining an approximate flow field of the continuous phase (airflow in this study), droplets are injected, and their trajectories are calculated. At the same time, drag, heat and mass transfer between the droplets and the airflow are calculated.

Iteration proceeded alternatively between the continuous and discrete phases. Twenty iterations in the continuous phase are conducted between two consecutive iterations in the discrete phase. Converged results were obtained after the specified residuals are met. A converged result renders mass residual of 10^{-3}, energy residual of 10^{-6}, and momentum and turbulence kinetic energy residuals of 10^{-3}. These residuals are the summation of the imbalance for each cell and scaled by a representative of the flow rate. The transient time step is set for 0.1 millisecond for a total of 100 steps. For 3600 RPM rotating speed, this gives a total period of 0.01 second with a progress of 30 pitch passing. The time step is set in such a way that it becomes shorter than the time requires for the rotor to rotate a single pitch, which is 33.33 ms. Otherwise the discrete phase data won't be continuous in two consecutive pitch passings. Typically, 400 to 500 iterations are needed to obtain a converged result in each time steps, which takes about 90 hours in a cluster of 9 dual-core parallel personal computers.

Comparison of Different Turbulence Model and Time Constant

Comparison has been made among different turbulence model for baseline case and presented in Table 1. Static pressure and static temperature rise have been chosen as the comparing parameters. The computed result of static pressure rise is fairly consistent among different turbulent models, while the temperature rise calculations vary within 7%. According to Wang and Dhanasekaran [37], the time constant (C_t) used in stochastic tracking may significantly affect the results of particle tracking in certain flow conditions, so a sensitivity study is conducted to inspect its influence on the CFD results. Four different time constants, ranging from 0.15 to 0.0001, are used. Table 2 shows the results are consistent. The value of 0.15 is therefore used for all cases in this paper.

Table 1 Comparison among different turbulence models

Models	Parameters					
	Inlet Static Press. (kPa)	Exit Static Press. (kPa)	**Static Pressure Ratio**	Inlet Static Temp. (K)	Exit Static Temp. (K)	**Temp. Diff (K)**
Spalart Almaras	95.85	108.00	**1.12672**	299.40	311.46	**12.06**
k-ε Standard	96.30	108.00	**1.12154**	299.79	311.88	**12.09**
k-ε RNG	95.77	108.00	**1.12770**	299.32	311.31	**11.98**
k-ε Realizable	95.72	108.00	**1.12828**	299.28	311.24	**11.96**
k-ω Standard	96.09	108.00	**1.12389**	299.61	311.52	**11.91**
k-ω SST	95.66	108.00	**1.12904**	299.22	311.19	**11.97**

Table 2 Comparison among different time constants used in stochastic particle tracking scheme

Models	Parameters					
	Inlet Static Press. (kPa)	Exit Static Press. (kPa)	**Static Pressure Ratio**	Inlet Static Temp. (K)	Exit Static Temp. (K)	**Temp. Diff (K)**
$C_t = 0.15$	96.37	107.90	**1.11966**	299.89	310.95	**11.06**
$C_t = 0.01$	96.37	107.90	**1.11960**	299.89	310.96	**11.06**
$C_t = 0.001$	96.38	107.90	**1.11958**	299.89	310.97	**11.07**
$C_t = 0.0001$	96.37	107.90	**1.11959**	299.89	310.96	**11.06**

Comparison of Results using Different Mesh size

A grid sensitivity study is made for the baseline case. Four different sizes of mesh are used, e.g. 0.25, 0.47, 0.9 and 1.67 million elements are used, i.e. each time the mesh size has been doubled, which gives almost 25% excess nodes than the smaller one. Table 3 shows the sensitivity result. Pressure rise is almost grid independent (only 0.05% off from coarsest grid). However, temperature rise is little off from the coarsest grid. It is found that the temperature rise is 3% off for 0.47 million elements than the coarsest (0.25 million) one. It is 6.2% off for 0.9 million elements than the coarser (0.47 million) one and so on. Due to the computational limitations, it was not possible to increase the grid size.

Table 3 Comparison among different mesh numbers

Number of mesh elements	Parameters							
	Inlet Static Press. (kPa)	Exit Static Press. (kPa)	**Static Press. Ratio**	**Diff. from smaller mesh**	Inlet Static Temp. (K)	Exit Static Temp. (K)	**Temp. Diff. (K)**	**Diff. from smaller mesh**
252,733	96.30	108.00	**1.1215**		299.79	311.88	**12.09**	
467,392	96.24	108.00	**1.1222**	**0.05%**	300.31	312.76	**12.45**	**3.02%**
906,761	96.21	108.00	**1.1226**	**0.04%**	300.28	313.50	**13.22**	**6.19%**
1,670,128	96.18	108.00	**1.1229**	**0.03%**	300.26	314.71	**14.45**	**9.28%**

RESULTS AND DISCUSSION

Studied Cases

1. Baseline case: No fogging. Moist air compression (conventionally called dry compression even though there is moisture in the air) with the ambient air at 300K, 60% RH, and 1 bar pressure.
2. Fog cooling case: Ambient condition is the same as the baseline case with 1% overspray of 288K water.

In this study, the term "fogging" indicates the action of generating the fog. Depending on the amount of injected water, "saturation fogging" implies the process of saturating

the air to 100% relative humidity and "overspray" implies the process of injecting more than the water amount required to achieve saturated air. Strictly speaking, a 1% overspray implies the amount of water that weighs 1% of the dry air flow is injected, in addition to the amount required to saturate the air. However, for simplicity, overspray fogging also includes saturation fogging in this study. For example, 1% water overspray with an ambient condition of 300K and 60% RH implies that 0.245% water is needed to saturate the air, and $(1 - 0.245) = 0.755\%$ is actually used for overspray.

The term "moist air compression" indicates that no liquid is in the air, but the air humidity is not zero. "Wet compression" means liquid droplets present in the air during compression.

Static Pressure Result

Compressor's static pressure increases from 96.2 kPa to 108 kPa with a static pressure ratio 1.123 for the baseline case as shown in Fig. 5(a). The lowest static pressure (suction peak) at 81 kPa is found on the suction side of the rotor near the leading edge. The stagnation pressure in the range of 113 and 128 kPa is found at the stagnation region of rotor shown in Fig. 5(b). The static pressure in 3 different radial planes for baseline case does not show any significant difference and neither does in the fogging case.

As fogging is applied, compressor's static pressure increases from 96.4 kPa at inlet to 107.9 kPa with a static pressure ratio of 1.119 as shown in Fig. 5(c), a bit lower than baseline case. When fogging is applied, the stagnation line has not been shifted significantly (see Fig. 5(d)). The stagnation pressure ranges from 115 to 128 kPa for baseline case (Fig. 5(b)) and 110 to 121 kPa for the fogging case at the stagnation line. The isobar contours for the fogging case and baseline case do not show any significant difference. The intuition says that the pressure ratio should increase due to fogging according to thermodynamic study. The fogging case in this study does not complete evaporation, so the pressure ratio is not improved in this single stage.

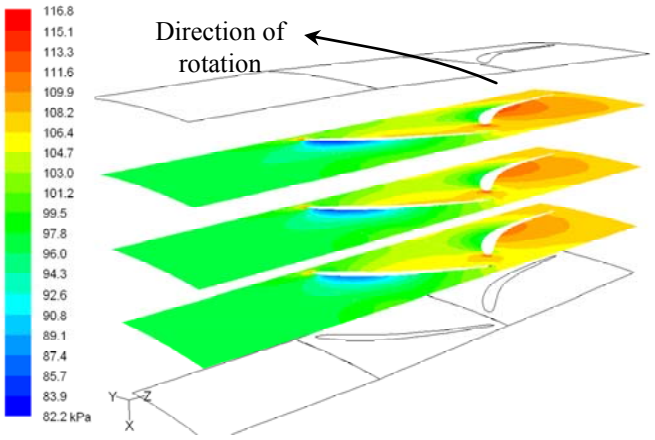

Figure 5 (a) Static pressure distribution for baseline case in different radial planes

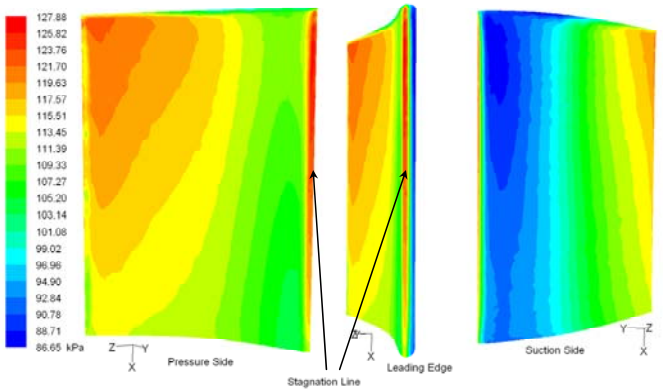

Figure 5 (b) Stagnation pressure distribution on the rotor surface for baseline on suction surface, leading edge, and pressure surface.

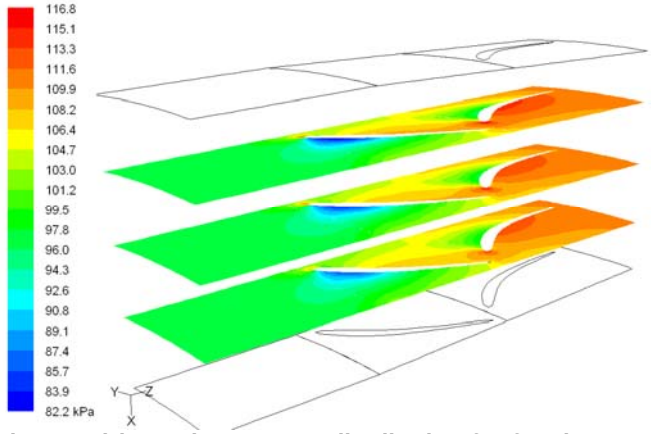

Figure 5 (c) Static pressure distribution for fogging case on different radial planes and over the hub.

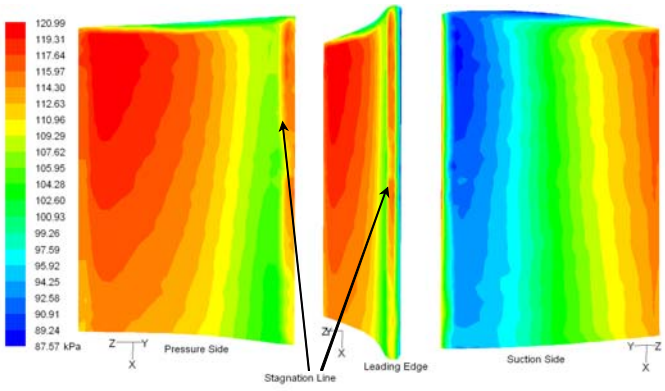

Figure 5 (d) Stagnation pressure distribution for fogging case across the rotor surface

Static Temperature Results

The temperature distribution without and with water spray is shown in Figs. 6(a) and (b). For baseline case (dry air with 60% relative humidity without fogging), a wide range of temperature distribution is noticed. Inlet portion is more uniform (in the range of 300 to 304K). Temperature significantly drops to 288K at the leading edge of suction side of rotor due to strong acceleration and pressure drop downstream of the stagnation region (see Fig. 5a).

Temperature increases from 288K to 308K along the suction side and from 304K to 311K along the pressure side. As expected, the static pressure is higher on the pressure (convex) side and lower on the suction (concave) side as shown in Fig. 5(a), and due to the nature of compression, air temperature is higher on the pressure side and lower on the suction side (Fig. 6). The average temperature is 314.7K at the exit.

For the fogging case (Fig. 6b), the temperature drops from the baseline case. The temperature is higher on the pressure side and lower on the suction side for both the rotor and stator for the fogging case. In addition, the temperature reduces to 311K at the exit. The temperature significantly drops to 289K at the leading edge of suction side of rotor due to strong acceleration and pressure drop downstream of the stagnation region (see Fig. 5b). Also, the temperature increases from 289K to 305K along the suction side and from 305K to 309K along the pressure side.

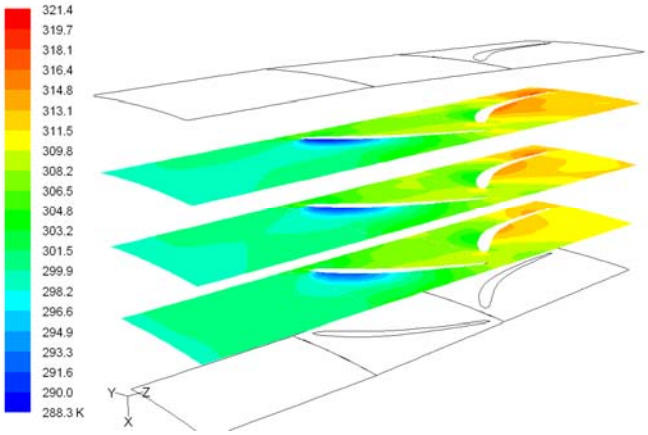

Figure 6 (a) Static temperature distribution for baseline case (no fogging) on three radial planes

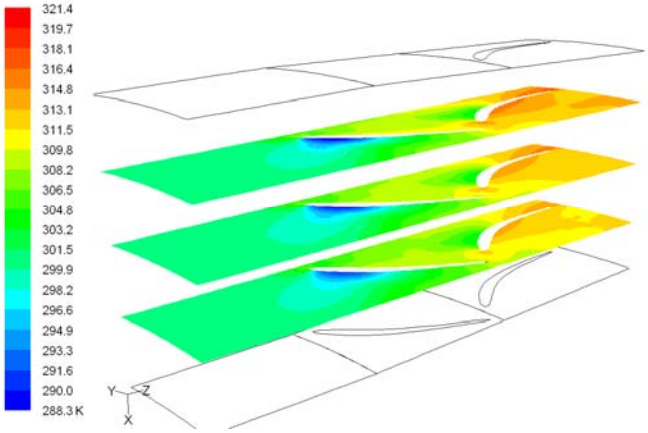

Figure 6 (b) Temperature distribution for fogging case on different radial planes and hub surface

Velocity Results

The inlet velocity at rotor is 92 m/s for the baseline case and 93.5 m/s for fogging case. The exit velocity at the rotor is approximately 136.5 m/s for baseline case and 137 m/s for fogging case. There is a secondary flow moving from the pressure side towards the suction side as shown in Fig 7(a) and (b).

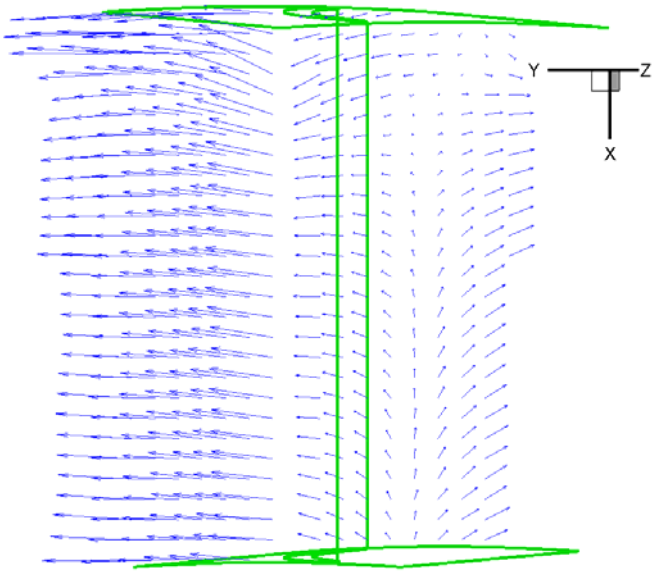

Figure 7(a) Secondary flow moving towards the suction surface at 20% chord length from the stator leading edge Data points are reduced for clarity. The main flow is moving into the paper. The plane of projection in this figure is the red (3rd) plane shown in Fig. 3.

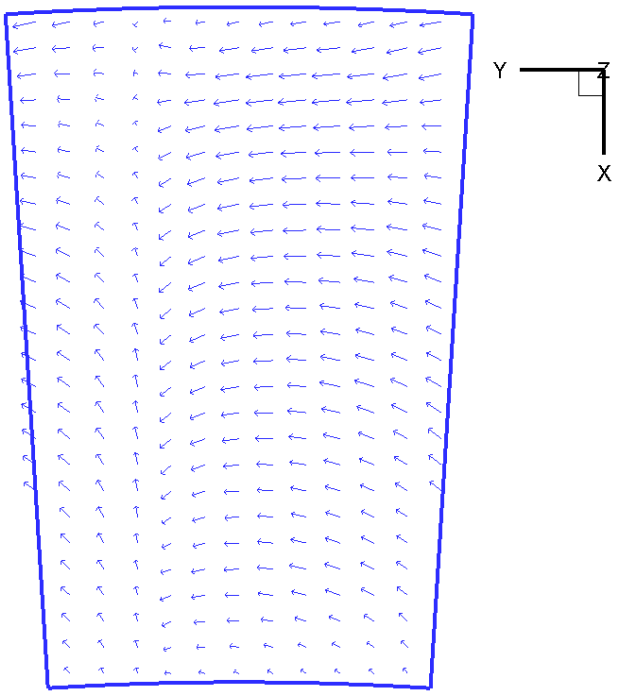

Figure 7(b) Secondary flow near the stator exit. Data points are reduced for clarity. The main flow is moving into the paper. The plane of projection in this figure is the black (rightmost) plane shown in Fig. 3.

Slip Velocity and Reynolds Number

Water droplets are injected at the inlet with the velocity of 25m/s along with the continuous phase (air) flowing at a

velocity of 92m/s. Initially the droplets have a slip velocity of -66m/s, which keeps decreasing (i.e. tends to zero) along the domain. This slip velocity affects the droplet Reynold's number and the associated drag and droplet evaporation rate. The variation of droplet Reynolds number is shown in Fig. 8. The droplet Reynolds number starts at around 15 at the inlet and reduces to almost zero at the end of the inlet sub-domain. As soon as the droplets enter the rotor sub-domain, they accelerate due to additional momentum from the rotational motion of the rotor and the induced centrifugal motion. As a result the droplet slip velocity increases from 0 to 40 m/s (as they move from leading to trailing edge of rotor) and a few particles are found to have a slip velocity more than 100m/s (droplet is faster than the air in rotor subdomain). Therefore, a slip Reynolds number in the range of 0 to 90 is observed. When the droplets enter the stator sub-domain, the slip velocity again decreases (as low as 5 m/s) and results in reduced droplet Reynolds number down to 7.

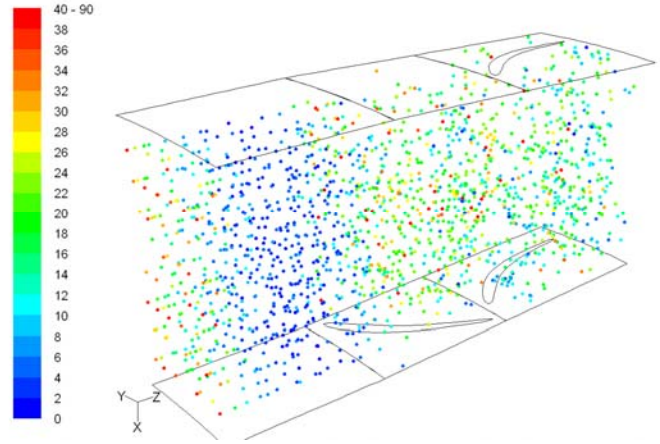

Figure 8 Water droplet trace with droplets' relative Reynolds number (one in every five droplets have been shown)

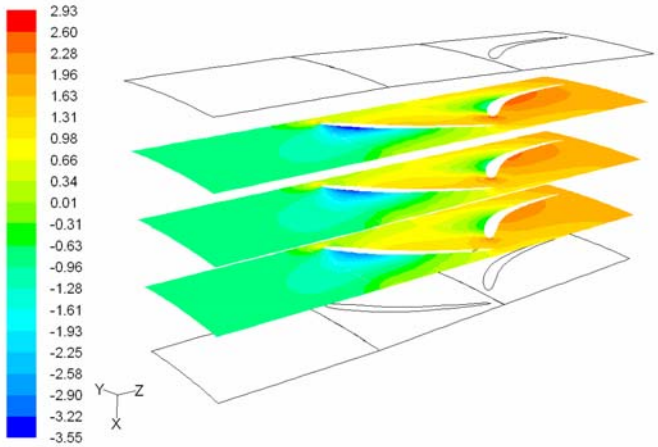

Figure 9(a) Contour of pressure coefficient on rotor and stator surfaces on three radial planes for the fogging case

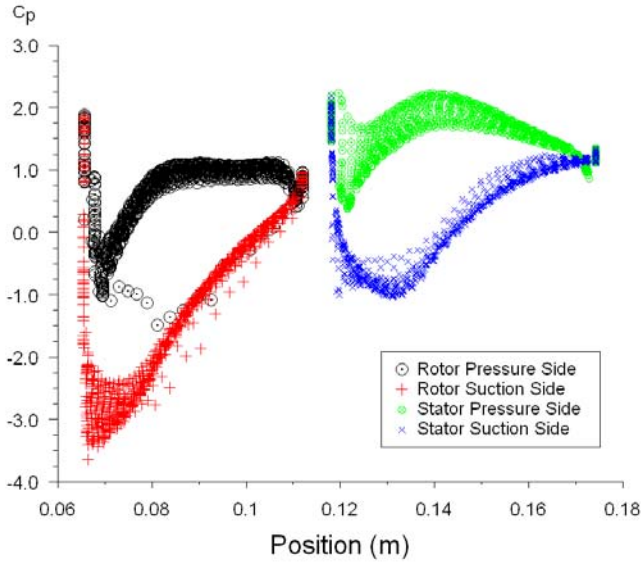

Figure 9(b) Variation of pressure coefficient across rotor and stator surfaces for the baseline case

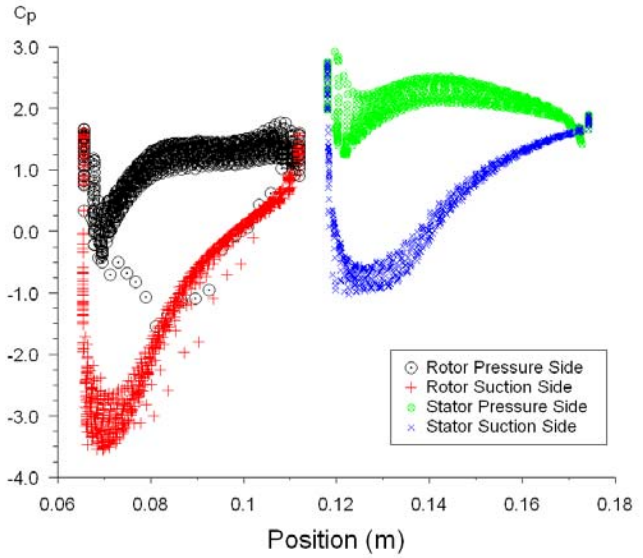

Figure 9(c) Variation of pressure coefficient across rotor and stator surfaces for the fogging case

Coefficient of Pressure

Figure 9(a) shows the contour of pressure coefficient [(P-Po)/(½ρv²)] on three radial planes in the fogging case and Figs. 9(b) and (c) show the pressure coefficient variation across the rotor and stator for all radial locations. It is obvious that the pressure side has higher pressure and suction side has less pressure. Only one line near the tip region in Figs. 9 (b) and (c) show relatively low pressure on the upper plane of the rotor pressure side due to the pressure leakage across the tip clearance. Only a slight difference in the distribution is observed between the dry and fogging cases.

Droplet Breakup and Coalescence

Droplet breakup and coalescence are considered in this study. Water droplet evaporation can occur anywhere in the domain. Droplet coalescence and break-up usually occur as a result of droplet collisions due to flow field changes through, for example, local acceleration/deceleration, centrifugal force, scattered movement of droplets or even turbulent dispersion.

Turbulent dispersion is noticed from the very beginning in the inlet domain, so the probability of collisions starts immediately after the water droplets are injected. It is obvious to observe that the droplet diameter does not increase without incorporating the coalescence model, the comparison with and without coalescence was presented by Khan and Wang [15]. The biggest size of the droplet found is 64.95µm (Fig. 10), which is created by the coalescence of 335 droplets of 10µm.

Figure 11 shows the liquid droplet concentration. At this periodic position, most of the liquid droplets hit the suction side and leave the pressure side uncooled. A little downward movement of the droplets is seen close to the exit of the rotor sub-domain (shown in Fig. 11a) and at the beginning of the stator sub-domain probably due to the secondary flow motion, which is clear from the secondary flow in Fig. 7(b).

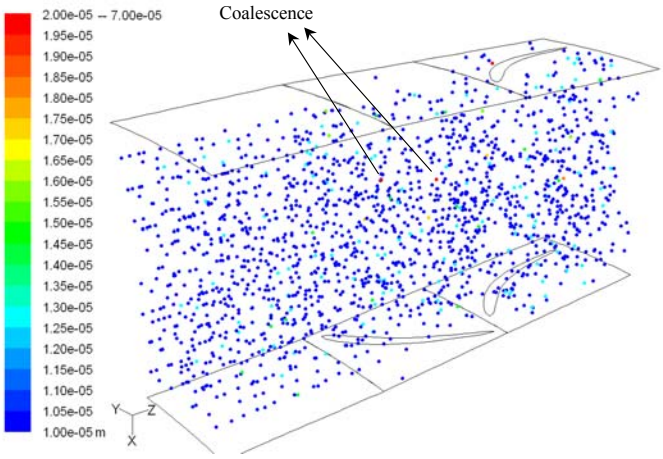

Figure 10 Water droplet trace with diameter. Red dots shows coalescence.

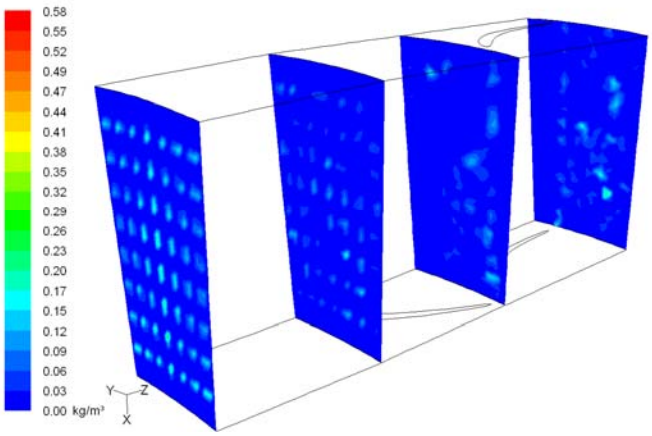

Figure 11(a) Liquid concentration on four different axial planes

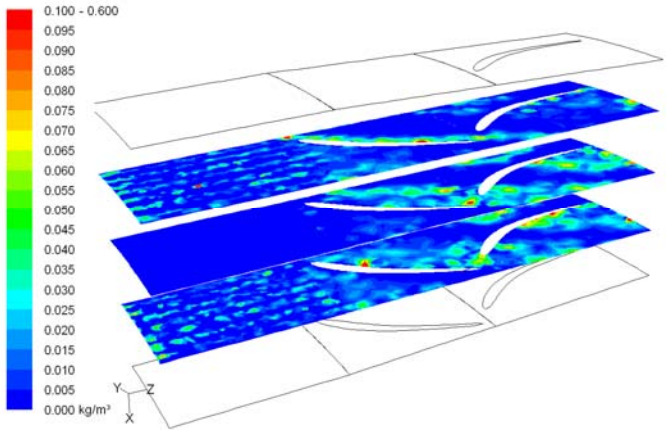

Figure 11(b) Liquid concentration on three different radial planes

Droplet Erosion

Figure 12 (a) shows the erosion on the rotor suction side and stator pressure side and Fig. 12(b) shows the erosion level on the rotor pressure side and stator suction side and the maximum erosion is quantified as 3.55×10^{-9} kg/m²s, which is equivalent to 14µm loss of material in one year given that the compressor runs 24 hours in 365 days a year. Based on current model, this erosion is pretty negligible. According to the boundary conditions, the spray is arranged at eight equidistant locations in radial direction. It is noticed that eroded areas are seen on the suction side in the rotor leading edge and a big pit on the trailing edge due to a secondary flow, which is clear from Fig. 7(b). Some droplets hit the stator's pressure side before leaving the domain (as shown by the secondary flow in Fig. 7a and 7b) and results in some erosion close to the trailing edge of the stator pressure side. Erosion on stator occurs mostly on the leading edge of the stator pressure side, as the rotor splashes the droplets towards the pressure side of the stator.

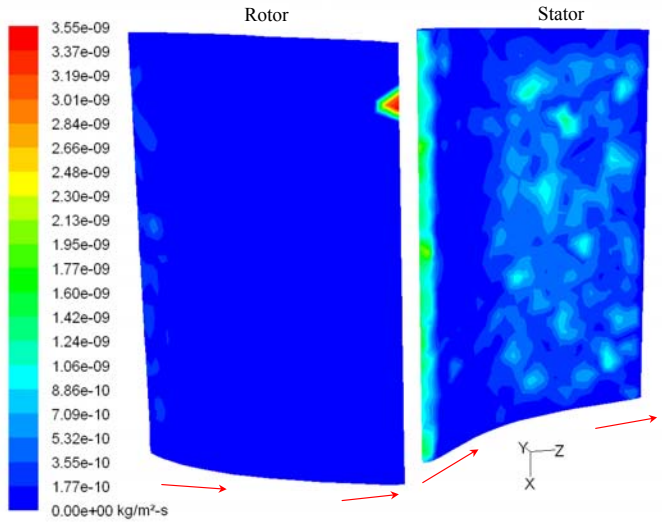

Figure 12 (a) Blade erosion on suction side of rotor and pressure side of stator. Red arrows show the flow direction.

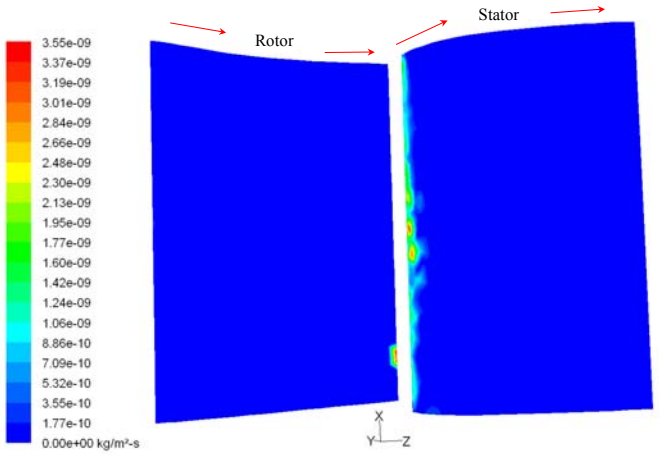

Figure 12 (b) Blade erosion on pressure side of rotor and Suction side of stator. Red arrows close to the surfaces show the flow direction.

CONCLUSIONS

CFD simulation has been performed on one rotor-stator stage of a compressor 3-D configuration with and without fogging. The summary of the findings is:

Under fogging, the temperature reduces, and the overall temperature distribution in the compressor becomes more uniform. The compressor exit temperature decreases from 314.7K to 311K with 1% overspray fogging. Under fogging, pressure ratio decreases from 1.123 to 1.119 and the axial velocity increases from 92 to 93.5m/s due to increased mass flow rate.

Most of the droplets reach main flow velocity (i.e. zero slip). Local pressure gradients in both the rotor and stator flow passages drive up the droplet slip velocity during compression. Most of the droplet relative Reynolds numbers are in the range of 30 to 50.

The CFD erosion model predicts that the most eroded area occurs in leading edge and one spot of trailing edge of the rotor suction side. The largest erosion rate is predicted as 3.55×10^{-9} (kg/m^2-s) or 0.112 (kg/m^2-yr), which is approximately equivalent to a loss of 14 μm thickness of metal layer per year, which is not significant, however this data needs validation from further experiments.

Consistency is obtained among six different turbulent models and four different stochastic tracking time constants except the k-ω Standard model is a bit off from all other models.

ACKNOWLEDGEMENT

This study was supported by the Louisiana Governor's Energy Initiative via the Clean Power and Energy Research Consortium (CPERC) and administrated by the Louisiana Board of Regents.

REFERENCES

1. Cortes, C.R. and Willems, D.E., 2003, "Gas Turbine Inlet Air Cooling Techniques: An Overview of Current Technologies," POWER-GEN, Las Vegas, Neva, USA.
2. Bhargava, R. and Meher-Homji, C.B., 2005, "Parametric Analysis of Existing Gas Turbines With Inlet Evaporative and Overspray Fogging," Journal of Engineering for Gas Turbines and Power, January 2005, Vol. 127, pp. 145-158.
3. Chaker, M., Meher-Homji, C.B., Mee, T.R., 2004, "Inlet Fogging of Gas Turbine Engines—Part I: Fog Droplet Thermodynamics, Heat Transfer, and Practical Considerations," Journal of Engineering for Gas Turbines and Power, July 2004, Vol. 126, pp. 545-558.
4. Chaker, M., Meher-Homji, C.B., Mee, T.R., 2004, "Inlet Fogging of Gas Turbine Engines—Part II: Fog Droplet Sizing Analysis, Nozzle Types, Measurement, and Testing," Journal of Engineering for Gas Turbines and Power, July 2004, Vol. 126, pp. 559-570.
5. Chaker, M., Meher-Homji, C.B., Mee, T.R., 2004, "Inlet Fogging of Gas Turbine Engines—Part III: Fog Behavior in Inlet Ducts, Computational Fluid Dynamics Analysis, and Wind Tunnel Experiments," Journal of Engineering for Gas Turbines and Power, July 2004, Vol. 126, pp. 571-580.
6. Payne, R.C. and White, A. J., 2008, "Three-Dimensional Calculations of Evaporative Flow in Compressor Blade Rows," Journal of Engineering for Gas Turbines and Power, May 2008, Vol. 130, pp. 032001-1—032001-6
7. Bianchi, M., Melino, F., Peretto, A., Spina, P.R. and Ingistov S., 2007, "Influence of Water Droplet Size and Temperature on Wet Compression," Proceedings of ASME Turbo Expo 2007, Montreal, Canada, May 14-17, 2007, ASME Paper No: GT2007-27458.
8. Khan, J.R. and Wang, T., 2006, "Fog and Overspray Cooling for Gas Turbine Systems with Low Calorific Value Fuels," Proceedings of ASME Turbo Expo 2006, Barcelona, Spain, May 8-11,ASME Paper GT2006-90396.
9. Wang, T. and Khan, J.R., 2008, "Overspray and Interstage Fog Cooling in Compressor using Stage-Stacking Scheme -- Part 1: Development of Theory and Algorithm," presented at the ASME Turbo Expo2008, Berlin, Germany, June 9-13, 2008, ASME Paper: GT2008-50322.
10. Wang, T. and Khan, J.R., 2008, "Overspray and Interstage Fog Cooling in Compressor using Stage-Stacking Scheme -- Part 2: A Case Study," presented at the ASME Turbo Expo2008, Berlin, Germany, June 9-13, 2008, ASME Paper No: GT2008-50323.
11. Khan, J.R., and Wang, T., 2009, "Overspray Fog Cooling in Compressor using Stage-Stacking Scheme with Non-Equilibrium Heat Transfer Model for Droplet Evaporation" presented at the ASME Turbo Expo2009, Orlando, Florida, USA, June 8-12, 2009, ASME Paper GT2009-59590.
12. Li, X., and Wang, T., 2007, "Effects of Various Modelings on Mist Film Cooling," ASME Journal of Heat Transfer, vol. 129, pp. 472-482.
13. Wang, T. and Dhanasekaran, T.S., 2008, "Calibration of CFD Model for Mist/Steam Impinging Jets Cooling," Proceedings of ASME Turbo Expo 2008, Berlin, Germany, June 9-13, 2008, ASME Paper No: GT2008-50737.
14. Zheng, Q., Shao, Y. and Zhang, Y., 2006, "Numerical Simulation of Aerodynamic Performances of Wet

Compression Compressor Cascade," ASME GT2006-91125.
15. Khan, J. R., and Wang, T., 2008, "Simulation of Inlet Fogging and Wet-compression in a Single Stage Compressor Including Erosion Analysis," Proceedings of ASME Turbo Expo2008, Berlin, Germany, June 9-13, 2008, ASME Paper No: GT2008-50874.
16. Hsu, S. T., and Wo, A. M., 1998, "Reduction of Unsteady blade Loading by Beneficial Use of Vortical and Potential Disturbances in an Axial Compressor with Rotor Clocking," ASME J. Turbomach., 120, pp. 705–713.
17. Chima, R.V., 1998, "Calculation of Tip Clearance Effects in a Transonic Compressor Rotor," Journal of Turbomachinery, January 1998, Vol. 120, pp. 131-140.
18. Gerolymos, G.A. and Vallet, I., 1999, "Tip-Clearance and Secondary Flows in a Transonic Compressor Rotor," Journal of Turbomachinery, October 1999, Vol. 121, pp. 751-762.
19. Launder, B. E. and Spalding, D. B., 1972, Lectures in Mathematical Models of Turbulence, Academic Press, London, England.
20. Wolfstein, M., 1969, "The Velocity and Temperature Distribution of One-Dimensional Flow with Turbulence Augmentation and Pressure Gradient," Int. J. Heat Mass Transfer, 12, pp. 301-318.
21. Wang, S., Liu, G., Mao, J., and Feng, Z., 2007, "Experimental Investigation on the Solid Particle Erosion in the Control Stage Nozzles of Steam Turbine," Proceedings of ASME Turbo Expo 2007, Montreal, Canada, May 14-17, 2007, ASME Paper: GT2007-27700.
22. Schiller, L., and Naumann, A., 1933, "Uber die grundlegenden Berechnungen bei der Schwekraftaubereitung," Zeitschrift des Vereines Deutscher Ingenieure, 77(12), 318-320.
23. Ranz, W. E. and Marshall, W. R. Jr., 1952, "Evaporation from Drops, Part I," Chem. Eng. Prog., 48, pp. 141-146.
24. Ranz, W. E. and Marshall, W. R. Jr., 1952, "Evaporation from Drops, Part II," Chem. Eng. Prog., 48, pp. 173-180.
25. Kuo, K. Y., 1986, *Principles of Combustion*, John Wiley and Sons, New York.
26. O'Rourke, P. J. and Amsden, A. A., 1987, "The Tab Method for Numerical Calculation of Spray Droplet Breakup," SAE Technical Paper 872089, 1987.
27. O'Rourke, P. J., 1981, "Collective Drop Effects on Vaporizing Liquid Sprays," PhD dissertation, Princeton University, New Jersey, 1981.23.
28. Lam, T. C-T. and Dewey, R., 2003, "A Study of Droplet Erosion on Two L-0 Turbine Stages," Proc. of IJPGC 2003, Atlanta, Georgia, USA, June 16-19, IJPGC Paper No: IJPGC2003-40082.
29. Haugen, K., Kvernvold, O., Ronold, A. and Sandberg, R., 1995, "Sand erosion of wear-resistant materials: Erosion in choke valves," Wear 186-187, pp. 179-188.
30. Nokleberg, L. and Sontvedt, T., 1998, "Erosion of Oil and Gas Industry Choke Valves Using Computational Fluid Dynamics and Experiment," International Journal of Heat and Fluid Flow, 19, pp. 636-643.
31. Bowden, F.P. and Field, J.E., 1964, "The Brittle Fracture of Solids by Liquid Impact, by Solid Impact, and by Shock", Proceedings of the Royal Society (London) A, Vol 282, 1964, pp. 331-352.
32. Keating, A. and Nesic, S., 1999, "Prediction of Two-Phase Erosion-Corrosion in Bends," Second International Conference on CFD in the Minerals and Process Industries, CSIRO, Melbourne, Australia, December 6-8, 1999, pp. 229-236.
33. Bitter, P.P.A., 1963, "A Study of Erosion Phenomena, Part I", Wear, 6.
34. Bitter, P.P.A., 1963, "A Study of Erosion Phenomena, Part II", Wear, 6.
35. Guo, T., Wang, T. and Gaddis, J. L., 2000, "Mist/Steam Cooling in a Heated Horizontal Tube – Part 2: Results and Modeling," Transactions of the ASME, Vol. 122, 366-374.
36. Fluent Manual, Version 6.3, 2008, Fluent, Inc.
37. Wang, T. and Dhanasekaran, T. S., "Calibration of CFD Model for Mist/Steam Impinging Jets Cooling," ASME Paper GT2008-50737, presented at the ASME Turbo Expo2008, Berlin, Germany, June 9-13, 2008.